International Journal of Solids and Structures 49 (2012) 3047–3054

Contents lists available at SciVerse ScienceDirect

International Journal of Solids and Structures

journal homepage: www.elsevier.com/locate/ijsolstr

Effect of stress-state and spacing on voids in a shear-field

Viggo Tvergaard

Department of Mechanical Engineering, Solid Mechanics, Technical University of Denmark, DK-2800 Kgs. Lyngby, Denmark

ARTICLE INFO

Article history:
Received 1 November 2011
Received in revised form 11 June 2012
Available online 27 June 2012

Keywords:
Voids
Shear failure
Plasticity
Large strains
Contact

ABSTRACT

Unit cell model analyses are carried out for a material with a periodic array of voids, subject to shear loading. Thus the focus is on ductile fracture in conditions of low stress triaxiality. It has been shown recently that voids in shear are flattened out to micro-cracks, which rotate and elongate until interaction with neighboring micro-cracks gives coalescence, so that the failure mechanism is very different from that under tensile loading. In the present studies the plane strain unit cell has fully periodic boundary conditions, so that any combination of the stress components in the overall average stress state can be prescribed. This also allows for studies of the effect of different initial void spacing in the two in-plane coordinate directions. The stress states considered are essentially simple shear, with various levels of tensile stresses or compressive stresses superposed, i.e. low positive stress triaxiality or even negative stress triaxiality. For high aspect ratio unit cells a clear localization band is found inside the cell, which actually represents several parallel bands, due to periodicity. In the materials represented by a low aspect ratio unit cell localization would also occur after that the maximum shear stress has been passed, but this is not shown when periodicity is enforced. The effect of superposed tensile or compressive stresses is found to be bigger for high aspect ratio unit cells than for low aspect ratios.

1. Introduction

When voids deform in a ductile material subject to hydrostatic tension the void volumes tend to grow large and ductile failure occurs by coalescence of neighbouring voids (see reviews by Garrison and Moody, 1987; Tvergaard, 1990; Benzerga and Leblond, 2010). This mode of failure is reasonably well described by a number of micromechanical models (Gurson, 1977; Tvergaard, 1981; Gologanu et al., 1997; Danas and Castaneda, 2009a,b; Keralavarma and Benzerga, 2010). In these models the prediction of ductile failure depends on void growth, but in simple shear where the hydrostatic tension is zero, there is no void growth. For materials undergoing shear deformations with low or even negative hydrostatic tension the mechanism leading to failure is different. Thus, Fleck and Hutchinson (1986) have found for an initially spherical void in a linearly viscous material under remote shearing that the void becomes ellipsoidal, rotates, and finally forms a penny-shaped crack. Recent micro-mechanical studies by Tvergaard (2008, 2009) for a material containing a row of circular cylindrical voids subject to simple shear have shown that the voids are flattened out to micro-cracks, which rotate and elongate until interaction with neighbouring micro-cracks gives coalescence. Thus, also in shear ductile failure occurs due to the deformation of voids and their interaction with neighbouring voids, but the mechanism is very different from the well-known void growth to coalescence mechanism under tensile loading.

In Tvergaard (2008) the void closure was accounted for in an approximate manner, by using an internal hydrostatic pressure to simulate the crack surface contact, with the pressure level continuously adjusted such that the aspect ratio of the flattened void does not pass a specified limiting value. The approximation is made to avoid numerical complications in a full analysis of a completely closed crack with crack surface contact and with much material flow around the crack tips. Also Tvergaard (2009) applied an internal load on the void surface to approximately model contact by frictionless sliding, but here the internal loading was chosen normal to a plane along the elongated void such that no load component would tend to increase the length of the void and thus unrealistically enhance the shear mechanism of ductile failure. These studies include cases where shearing occurs under a superposed hydrostatic tension or a superposed hydrostatic pressure. Very recently, Dahl et al. (2012) have carried out analyses with full numerical contact modelling, which have confirmed that the procedure of Tvergaard (2009) gives a very good approximation to the condition of contact with frictionless sliding.

The elastic–plastic shear specimen containing a row of circular cylindrical voids has been analyzed earlier by Fleck et al. (1989) to model experiments of Cowie et al. (1987), in which the shear loading was combined with tension or compression and failure tended to occur by shear localization and void sheet fracture Barsoum and Faleskog (2007a) have carried out full 3D analyses for similar shear specimens containing spherical voids in order to model their experiments (Barsoum and Faleskog, 2007b) on ductile fracture

E-mail address: viggo@mek.dtu.dk

0020-7683/$ - see front matter © 2012 Elsevier Ltd. All rights reserved.
http://dx.doi.org/10.1016/j.ijsolstr.2012.06.008

in a double notched tube specimen loaded in combined tension and torsion. Initially spheroidal voids in a shear field have also been analyzed by Scheyvaerts et al. (2006), and 3D analyses for voids in shear fields have been carried out by Leblond and Mottet (2008). None of these studies have been continued into the important range where the voids have become micro-cracks that continue interacting. However, Anderson et al. (1990), considering the effect of a row of micro-cracks in a material subject to shear, have shown that localization can result from crack rotation and stretching.

An extension of the Gurson model has been proposed by Nahshon and Hutchinson (2008) to be able to describe failure in simple shear where the hydrostatic tension is zero. In this extended model the damage parameter is no longer a geometrically well defined void volume fraction, so this aspect of the model is more like continuum damage mechanics. Tvergaard and Nielsen (2010) have compared predictions of this shear-extended Gurson model with predictions of the micro-mechanical studies (Tvergaard, 2009) and have found that the trends of the predictions are in good agreement.

In the present paper the effect of the stress state and of the unit cell aspect ratio are studied for voids in a shear field. When the voids collapse to a micro-crack, the approximate description of Tvergaard (2009) for contact with frictionless sliding is still applied, but the interaction with neighbouring voids is not limited to a single row of voids, and the studies are not limited to cases with zero overall straining along the row of voids.

2. Problem formulation

While the shear specimen in previous studies contains a single row of voids along the x^1-axis, the materials studied here have a periodic array of voids, with the initial spacing $2A_0$ in the x^1-direction and the initial spacing $2B_0$ in the x^2-direction. This periodic array is analyzed by considering the unit cell in Fig. 1. Plane strain conditions are assumed and the voids are initially circular cylindrical with radius R_0. Finite strains are accounted for and the analyses are based on a convected coordinate Lagrangian formulation of the field equations, with a Cartesian x^i coordinate system used as reference. The metric tensors in the reference configuration and the current configuration, respectively, are g_{ij} and G_{ij} with determinants g and G, and $\eta_{ij} = 1/2(G_{ij} - g_{ij})$ is the Lagrangian strain tensor. The contravariant components τ^{ij} of the Kirchhoff stress tensor on the current base vectors are related to the components of the Cauchy stress tensor σ^{ij} by $\tau^{ij} = \sqrt{G/g}\sigma^{ij}$. A finite strain formulation for a J_2 flow theory material with the Mises yield surface is applied, where the incremental stress–strain relationship takes the form $\dot{\tau}^{ij} = L^{ijk\ell}\dot{\eta}_{k\ell}$, with the instantaneous moduli specified in (Hutchinson, 1973; Tvergaard, 1976). The true stress-logarithmic strain curve in uniaxial tension is taken to follow the power law

$$\varepsilon = \begin{cases} \sigma/E, & \sigma \leqslant \sigma_Y \\ (\sigma_Y/E)(\sigma/\sigma_Y)^{1/N}, & \sigma \geqslant \sigma_Y \end{cases} \tag{1}$$

with Young's modulus E, the initial yield stress σ_Y and the power hardening exponent N. Poisson's ratio is ν.

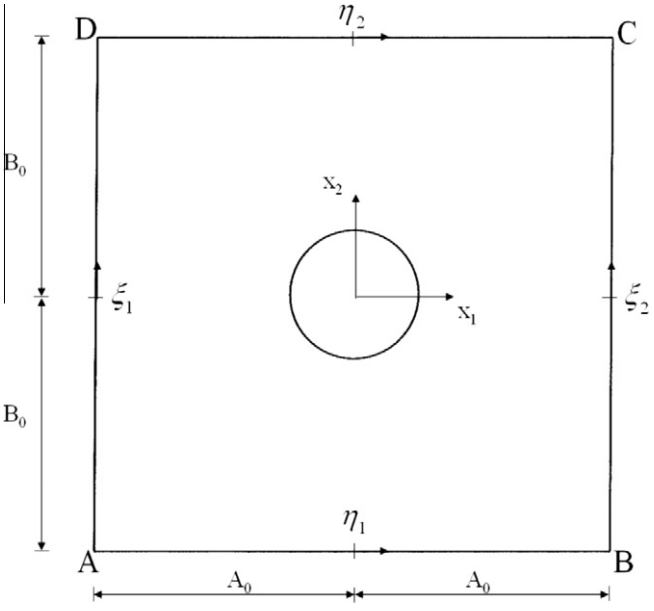

Fig. 1. Coordinates and dimensions for the unit cell analyzed.

Periodic boundary conditions on the unit cell model in Fig. 1 are required to be able to analyze the material with a doubly periodic array of voids, subject to shear. Thus, along the two sides of the unit cell the BC's are

$$u^1(\xi_1) - u^1_A = u^1(\xi_2) - u^1_B, \quad u^2(\xi_1) - u^2_A = u^2(\xi_2) - u^2_B, \tag{2}$$

$$T^1(\xi_1) = -T^1(\xi_2), \quad T^2(\xi_1) = -T^2(\xi_2), \tag{3}$$

where ξ_1 and ξ_2 are length measuring coordinates defined in Fig. 1. Along the top and the bottom of the unit cell the BC's are

$$u^1(\eta_1) - u^1_A = u^1(\eta_2) - u^1_D, \quad u^2(\eta_1) - u^2_A = u^2(\eta_2) - u^2_D, \tag{4}$$

$$T^1(\eta_1) = -T^1(\eta_2), \quad T^2(\eta_1) = -T^2(\eta_2), \tag{5}$$

where the parameters η_1 and η_2 are defined in Fig. 1. The displacements of the four corner points are denoted u^i_A, u^i_B, u^i_C and u^i_D, respectively. Rigid body translations are avoided by choosing $u^i_A = 0$, and then periodicity requires $u^i_C = u^i_D + u^i_B$. The remaining four free corner displacements determine the average deformation gradients for the unit cell, such that $F_{11} = 1 + u^1_B/2A_0$, $F_{22} = 1 + u^2_D/2B_0$, $F_{21} = u^2_B/2A_0$ and $F_{12} = u^1_D/2B_0$. In the present analyses only cases with $u^2_B = 0$ will be considered, such that $F_{21} = 0$.

A standard penalty method is used to approximately satisfy the relations (2)–(5) by taking

$$T^i(\xi_2) = k(u^i(\xi_2) - u^i(\xi_1) - u^i_B + u^i_A) = -T^i(\xi_1), \tag{6}$$

$$T^i(\eta_2) = k(u^i(\eta_2) - u^i(\eta_1) - u^i_D + u^i_A) = -T^i(\eta_1), \tag{7}$$

with the stiffness k chosen large enough to get a good approximation.

On a deformed unit cell the average directions of the side BC and the top CD are indicated by dashed lines in Fig. 2. The average normal and tangential vectors on BC, n^i_{BC} and t^i_{BC}, are indicated, as well as the average normal and tangential vectors, n^i_{CD} and t^i_{CD}, on CD. By integration of the nominal tractions the resultant forces in the coordinate directions are determined for BC and CD. From these forces and the current dimensions of the unit cell the average true stresses in the normal and tangential directions are determined, Σ^{BC}_n and Σ^{BC}_t on BC, and Σ^{CD}_n and Σ^{CD}_t on CD. Finally, using standard relations for these normal and tangential stress components, the Cartesian true stress components Σ_{11}, Σ_{22} and Σ_{12} are calculated. The numerical calculations are carried out such that fixed stress ratios are prescribed

$$\Sigma_{22}/\Sigma_{12} = \kappa, \quad \Sigma_{11}/\Sigma_{12} = \gamma \tag{8}$$

and the corresponding values of the corner displacements are calculated. In the results to be shown in Section 3, the average shear stress Σ_{12} is plotted against the deformation gradient F_{12}.

When the void deforms during shearing with low stress triaxiality, it will tend to close up into a micro-crack. The approximate method used here to model crack surface contact and frictionless sliding is that proposed in Tvergaard (2009). The length ℓ of the

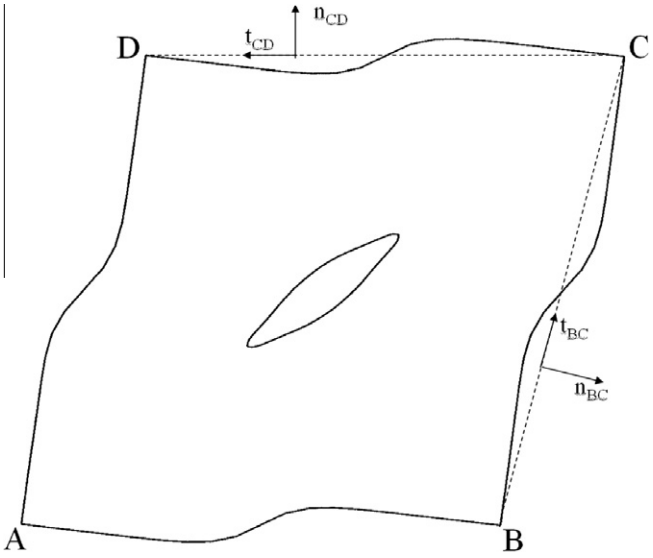

Fig. 2. Deformed unit cell indicating the average normal and tangential vectors used to define the average true stresses in the normal and tangential directions on the surfaces.

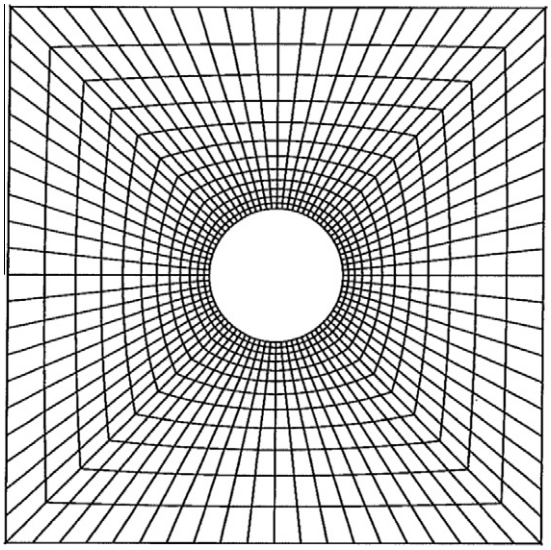

Fig. 3. Example of an initial mesh used for some of the numerical analyses.

ellipsoidal cross-section of the void is calculated as the largest distance between two surface points, and the average width w of the void is calculated from the current void volume V_v per unit length in the x^3 direction as $w = V_v/\ell$. Then, instead of a detailed representation of crack surface contact as the void develops into a micro-crack, the approximation is made that the average aspect ratio of the void is required to satisfy the inequality

$$w/\ell \geqslant \rho. \tag{9}$$

When the aspect ratio reaches the limit according to Eq. (9) an internal loading is applied to the void surface and this load is gradually increased so that the inequality (9) is not violated. The load on the void surface used by Tvergaard (2008) was a hydrostatic pressure. Subsequently, Tvergaard (2009) improved the approximation by using only the traction component perpendicular to the line of length ℓ between the two end points of the void, such that no load component will tend to increase the length of the void and thus unrealistically enhance the occurrence of ductile shear failure, which results from the fact that the micro-cracks rotate and elongate in the shear field until interaction with neighbouring micro-cracks gives failure.

3. Numerical method

The Lagrangian strain tensor is given in terms of the displacement components u^i on the reference base vectors as

$$\eta_{ij} = \frac{1}{2}\left(u_{i,j} + u_{j,i} + u^k_{,i}u_{k,j}\right), \tag{10}$$

where $(\,)_{,j}$ denotes covariant differentiation in the reference frame. The numerical solutions are obtained by a linear incremental solution procedure, based on the incremental principle of virtual work

$$\int_V \left\{\Delta\tau^{ij}\delta\eta_{ij} + \tau^{ij}\Delta u^k_{,i}\delta u_{k,j}\right\}dV = \int_A \Delta T^i \delta u_i dA - \left[\int_V \tau^{ij}\delta\eta_{ij}dV - \int_A T^i\delta u_i dA\right]. \tag{11}$$

Here, V and A are, respectively, the volume and surface of the body in the reference configuration, while $\Delta\tau^{ij}$ and $\Delta\eta_{ij}$ are the stress and strain increments. On the void surface the nominal tractions and their increments are specified as described below Eq. (9). The bracketed terms are equilibrium corrections. The displacement fields are approximated in terms of 8-noded isoparametric elements, and the volume integrals in (11) are carried out by using 2×2 point Gauss integration within each element. The periodicity conditions in the form (6) and (7) result in additional stiffness matrices, which are entered directly into the global stiffness matrix. An example of a mesh used for some of the numerical analyses is shown in Fig. 3.

Remeshing has been used here a few times in each computation, in order to avoid severe mesh distortion. In particular the flow of material around the sharp crack tips during shearing tends to give strong mesh distortion locally. The remeshing procedure applied was first introduced in one of the authors finite strain programmes by Pedersen (1998), and has been further developed in (Tvergaard, 1997, Tvergaard, 2004). The values of field quantities in the integration points of the new mesh are determined by interpolation in the old mesh. First, a bilinear surface in terms of the local element coordinates ξ and η is used to extrapolate values (such as stress components) in the old mesh from integration points to nodal points, where the region of the element is specified by $-1 \leqslant \xi \leqslant 1$ and $-1 \leqslant \eta \leqslant 1$. The stress values used for a nodal point are the averages of the values found by extrapolation from the adjacent elements. Then, values of the field quantities in the nodal points of the new mesh are determined by interpolation in the old mesh, using the shape functions. Finally, the values in the integration points of the new mesh are determined by interpolation from the new nodal points, using the shape functions. To do this, it is necessary to determine the location of each new nodal point in the old mesh, i.e. the element number and the appropriate values of the local coordinates ξ and η inside that element. This is done by repeated use of a Newton–Raphson iteration.

4. Results

The analyses are carried out for a material with $\sigma_Y/E = 0.002$, $\nu = 0.3$ and the strain hardening exponent $N = 0.1$. Different values are considered for the initial aspect ratio of the region analyzed, B_0/A_0, the initial void radius to width ratio, R_0/A_0, the stress ratios κ and γ in (8), and the limiting void aspect ratio ρ in (9). In most computations the value of the penalty parameter k in Eqs. (6) and (7) is chosen as $1000E/A_0$.

In the first comparison shown in Fig. 4 the cell model studies are carried out for $B_0/A_0 = 1$, $R_0/A_0 = 0.25$, $\rho = 0.15$ and $N = 0.1$. The value of κ is taken to be zero, such that $\Sigma_{22} = 0$, while the value of $\gamma = \Sigma_{11}/\Sigma_{12}$ is varied between -0.3 and 0.5. In addition one curve

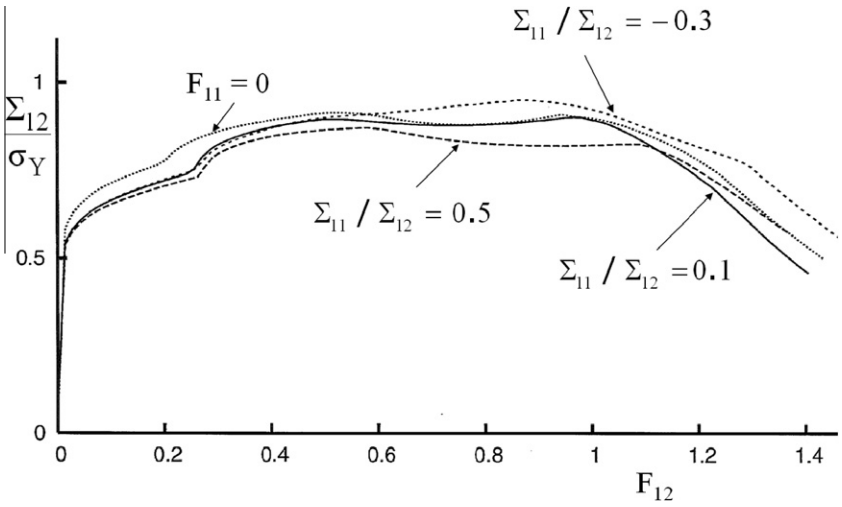

Fig. 4. Average shear stress vs. deformation gradient F_{12}, for $B_0/A_0 = 1$, $R_0/A_0 = 0.25$, $\rho = 0.15$ and $N = 0.1$. All curves have $\Sigma_{22} = 0$.

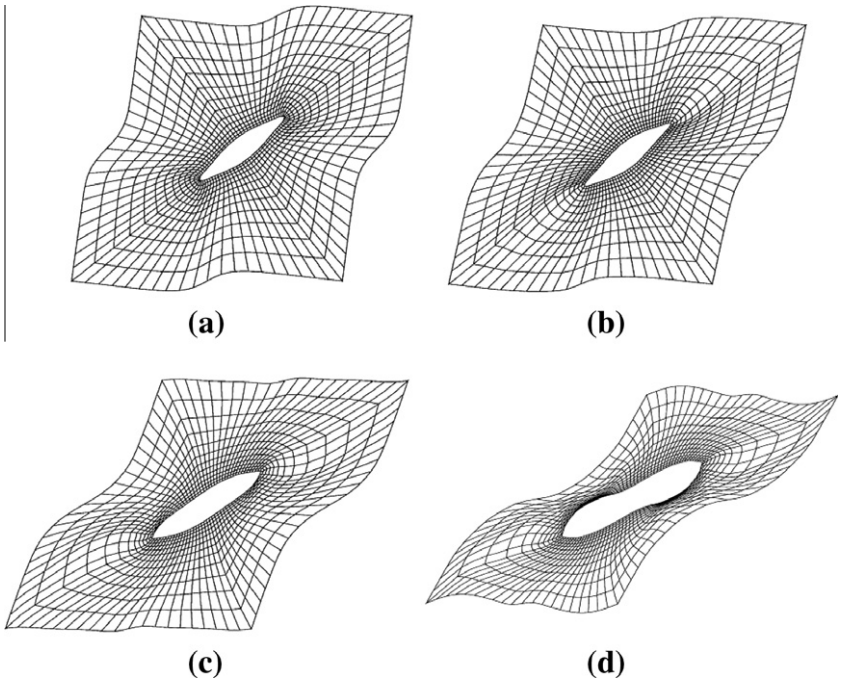

Fig. 5. Deformed meshes corresponding to the computation with $\Sigma_{11}/\Sigma_{12} = 0.1$ in Fig. 4. (a) At $F_{12} = 0.25$. (b) At $F_{12} = 0.35$. (c) At $F_{12} = 0.62$. (d) At $F_{12} = 1.12$.

is shown, for which the deformation gradient value $F_{11} = 0$ is specified instead of the value γ. The three curves for different values of γ are rather similar in shape. At $F_{12} \approx 0.25$ the curves show a characteristic kink in the point where crack surface contact initiates according to the approximate condition (9). Subsequently, while the crack surfaces remain in contact, there is a plateau with only moderate variations of the shear stress Σ_{12} while the overall shear strain grows large. At the end of the curves, in a range where F_{12} is between 1 and 1.4, the shear stress starts to decay markedly. The curve for $\Sigma_{11}/\Sigma_{12} = 0.5$ gives the lowest maximum shear stress, while the curve for $\Sigma_{11}/\Sigma_{12} = -0.3$ gives the highest maximum, but the difference is not very large. Also, it is seen that the curve for which zero straining in the x^1-direction, $F_{11} = 0$, is specified gives somewhat higher shear stress in the beginning, but is rather close to that for $\Sigma_{11}/\Sigma_{12} = 0.1$ when $F_{12} > 0.6$. The curves to be shown here depict the results in terms of Σ_{12} versus F_{12}, since the focus is on shear, but with a fixed ratio Σ_{11}/Σ_{12} the variation of Σ_{11} is easily seen from the curves.

For the computation with $\Sigma_{11}/\Sigma_{12} = 0.1$ in Fig. 4 deformed meshes at four different stages of the deformation are shown in Fig. 5. The stage in Fig. 5a, at $F_{12} = 0.25$, is immediately after that crack surface contact has initiated according to the approximate condition (9). In Fig. 5b, at $F_{12} = 0.35$, the crack has grown slightly longer, while at $F_{12} = 0.62$ the crack length is much increased. At the last stage illustrated, for $F_{12} = 1.12$, the micro-crack has become so long that it overlaps with the ends of the micro-cracks in the neighboring unit cells, and necking of the ligaments between neighboring crack ends has initiated. Due to this failure mechanism Fig. 5d corresponds to the range where the shear stress carried by the material decays rapidly.

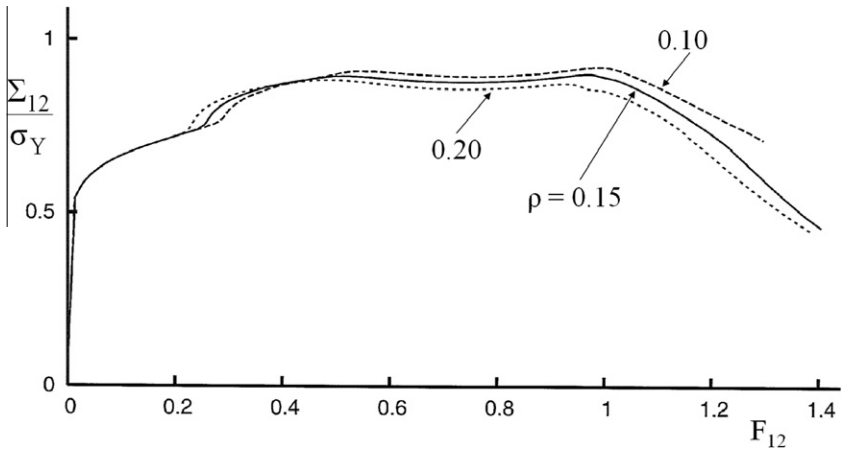

Fig. 6. Average shear stress vs. deformation gradient F_{12}, for $B_0/A_0 = 1$, $R_0/A_0 = 0.25$ and $N = 0.1$, with different values of ρ. All curves have $\Sigma_{22} = 0$.

The periodic pattern of micro-cracks, initiating from a periodic pattern of voids as represented by the unit cell calculations in Figs. 4 and 5, will not remain stable when the load maximum has been passed. Then a localization of plastic flow is expected, such that a shear band develops which involves continued plastic yielding around a row of micro-cracks, while elastic unloading would occur around the other micro-cracks. This type of deformation mode is not accounted for in the present unit cell calculations, since full periodicity is assumed throughout. However, a procedure for analyzing shear band localization from a periodic pattern of voids has been proposed by Tvergaard (1981).

In Fig. 5a and b the deformations of the top and bottom of the unit cell are nearly identical to the deformations of the sides of the unit cell, which shows that bands of more intense deformation have formed both through neighbouring voids in the horizontal direction and through neighbouring voids in the vertical direction. Fig. 5c and d show that the bands in the horizontal direction have become dominant, but the fact that the shapes of all edges of the unit cells still change indicates that there is not a larger region of elastic unloading. As mentioned above, crack surface contact by the model used has occurred in all of Fig. 5a–d, so the situation in Fig. 5d is that the micro-crack has grown so long relative to the unit cell size that ligaments between neighbouring micro-cracks in the horizontal direction have become very thin. If identical deformation of all unit cells was not enforced, some cells would undergo elastic unloading, thus leading to a clear localization band.

In Fig. 6 the effect of the limiting void aspect ratio ρ is studied by including curves for the values 0.10 and 0.20 in addition to the curve for $\rho = 0.15$, also shown in Fig. 4. All curves correspond to $\Sigma_{11}/\Sigma_{12} = 0.1$ and $\Sigma_{22} = 0$. The sharp kink in the curves near $F_{12} \approx 0.25$ occurs earlier for the larger value of ρ , indicating that this case finds earlier crack surface contact, as would be expected. Subsequently, the curve for $\rho = 0.10$, which gives the best approximation to actual crack surface contact, also results in the highest strength and in slightly later initiation of the final load decay.

The curve for $\Sigma_{11}/\Sigma_{12} = 0.1$, $\Sigma_{22} = 0$ and $R_0/A_0 = 0.25$, also shown in Figs. 4 and 6, is compared with predictions for relatively smaller voids in Fig. 7. The smaller voids result in a generally higher level of the shear stress Σ_{12} and in later occurrence of the last maximum before the final load decay. This tendency is as expected and also agrees with results found in Tvergaard (2008),Tvergaard, 2009 for a different unit cell and different stress state.

Variations of the aspect ratio B_0/A_0 of the unit cell are considered in Fig. 8. Again, the stress state $\Sigma_{11}/\Sigma_{12} = 0.1$ and $\Sigma_{22} = 0$, with $R_0/A_0 = 0.25$, is chosen as an example. These curves show a strong sensitivity to the unit cell aspect ratio, where the larger ratios $B_0/A_0 = 2$ and $B_0/A_0 = 4$ result in final failure at much smaller values of the deformation gradient F_{12} than that found for $B_0/A_0 = 1$. The reason is that the shear strain is not uniformly distributed in the unit cell, as was already seen in Fig. 5 on the deformed meshes for a unit cell with aspect ratio 1. It is clear in Fig. 5 that cross-sections through the void account for the major part of the shear straining represented by the average deformation gradient F_{12}. As has been discussed above, below Eq. (5), the average deformation gradients shown here are defined by the differences in the displacements at the four corners of the unit cell, in

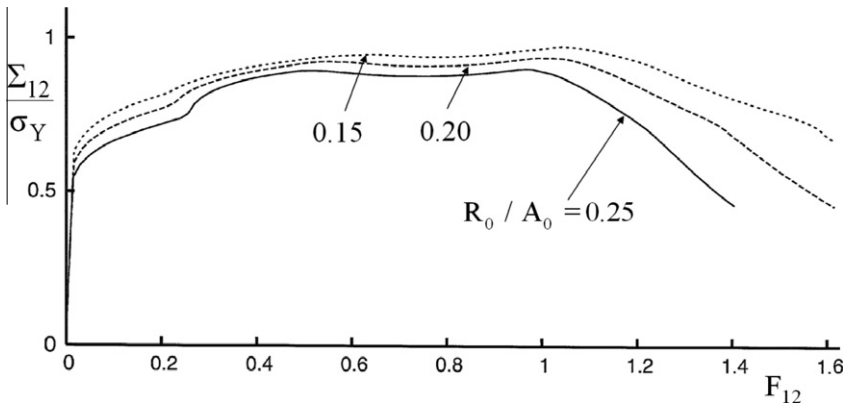

Fig. 7. Average shear stress vs. deformation gradient F_{12}, for $B_0/A_0 = 1$, $\rho = 0.15$ and $N = 0.1$, with different values of R_0/A_0. All curves have $\Sigma_{22} = 0$.

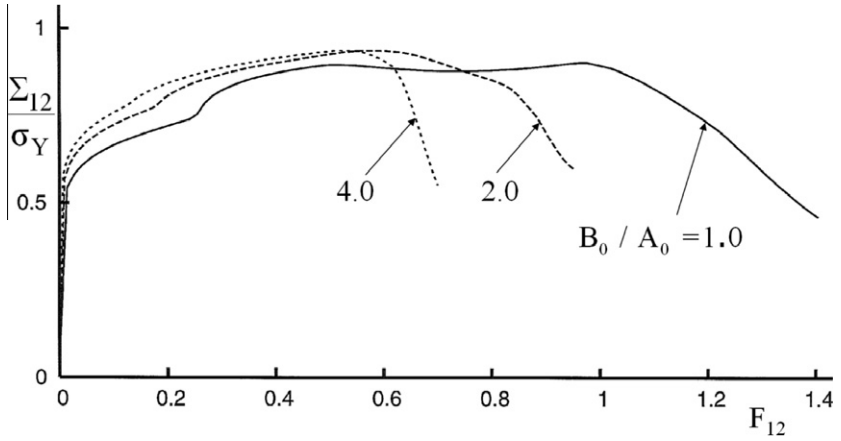

Fig. 8. Average shear stress vs. deformation gradient F_{12}, for $R_0/A_0 = 0.25$, $\rho = 0.15$ and $N = 0.1$, with different values of B_0/A_0. All curves have $\Sigma_{22} = 0$.

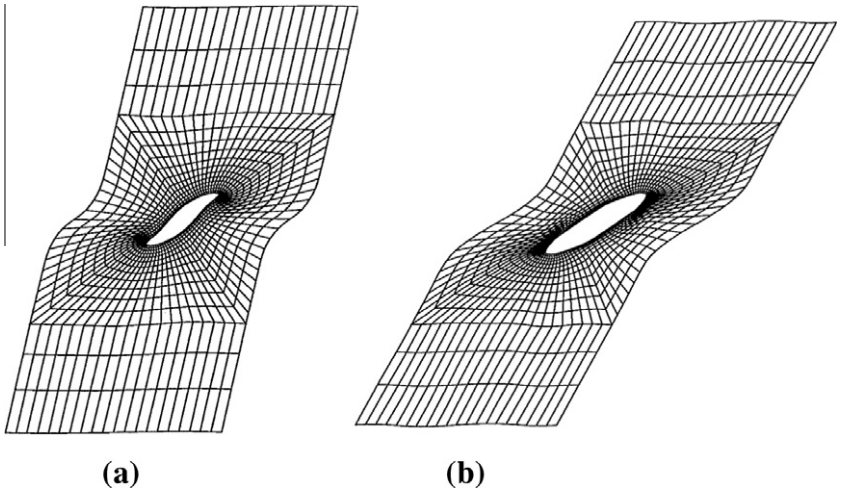

Fig. 9. Deformed meshes corresponding to the computation with $B_0/A_0 = 2$ in Fig. 8. (a) At $F_{12} = 0.31$. (b) At $F_{12} = 0.69$.

particular $F_{12} = (u_D^1 - u_A^1)/2B_0$. When considering the sides of the unit cell in Fig. 5 that were initially vertical, the average value F_{12} represents much less shearing than that found in the middle part of the unit cell but much more shearing than that found near the corners of the unit cell.

Fig. 9 shows the deformed meshes at two stages of the computation with $B_0/A_0 = 2$, illustrated by a curve in Fig. 8. On this curve the crack surface contact according to the approximate condition (9) initiated at $F_{12} = 0.18$. Thus, the stage shown in Fig. 9a, at $F_{12} = 0.31$, is well after initial crack closure. The stage shown in Fig. 9b, at $F_{12} = 0.69$, is a little after the maximum on the curve in Fig. 8. In Fig. 9b the crack has grown much longer than that shown in Fig. 9a, which is an important part of the shear failure mechanism studied here, where the cracks elongate and rotate in the shear field until neighboring crack ends are so close that failure occurs by necking of the ligament between two neighboring cracks. Comparing Figs. 9 and 5 it is seen that in Fig. 9a much larger part of the initially vertical sides of the unit cell experience the lower amount of shearing. Thus, for the same amount of shearing in the material just around the void, the unit cell with $B_0/A_0 = 2$ will show a lower value of the average deformation gradient F_{12}. This is the main reason why failure in Fig. 8 is predicted at a lower value of F_{12} for $B_0/A_0 = 2$ than for $B_0/A_0 = 1$ and at an even lower value for $B_0/A_0 = 4$.

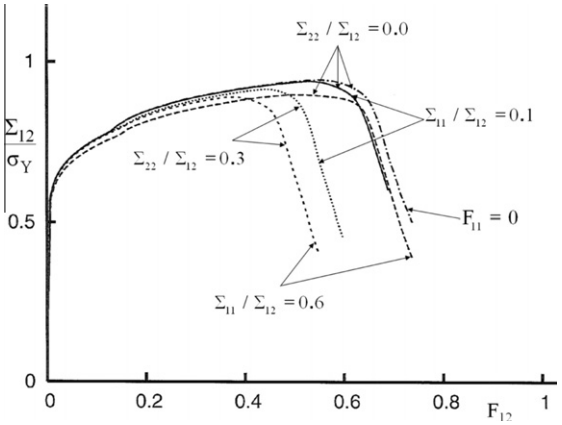

Fig. 10. Average shear stress vs. deformation gradient F_{12}, for $B_0/A_0 = 4$, $R_0/A_0 = 0.25$, $\rho = 0.15$ and $N = 0.1$, with different stress ratios.

The deformed meshes in Fig. 9 show that for the higher aspect ratio unit cell a plastic flow localization does develop in a band parallel to the x^1-axis, since at the end of the computation the parts of the unit cell near the top and the bottom have stopped deforming plastically. But the computation is still based on the assumption of

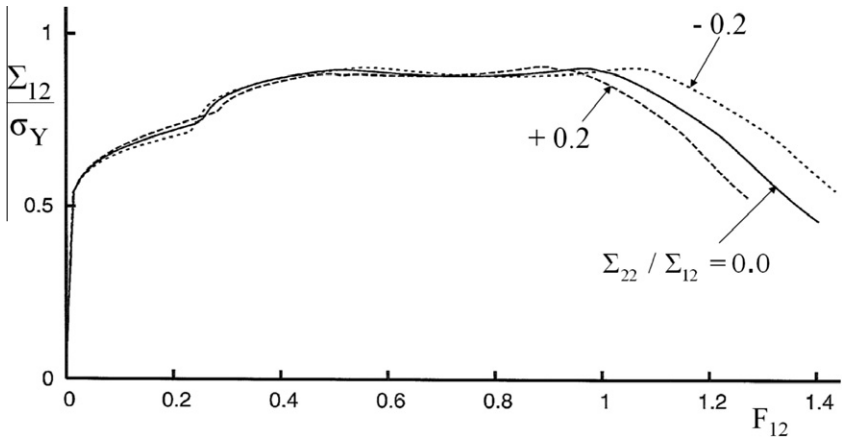

Fig. 11. Average shear stress vs. deformation gradient F_{12}, for $B_0/A_0 = 1$, $R_0/A_0 = 0.25$, $\rho = 0.15$ and $N = 0.1$, with different values of the stress ratio Σ_{22}/Σ_{12}.

periodicity, so that the deformed mesh in Fig. 9b actually represents a number of parallel shear bands containing parallel layers of micro-cracks.

The results in Fig. 8 clearly show a decrease in ductility for increasing aspect ratio of the unit cell. This is analogous to results of Koplik and Needleman (1988) for an axisymmetric unit cell with a single spherical void subject to rather high stress triaxiality. In both cases the deformations finally localize around the void, and this occurs at a smaller overall strain the larger the cell aspect ratio. Also, in both studies a much sharper decay of the load versus strain is found for the larger aspect ratio unit cell, where a relatively larger part of the cell undergoes elastic unloading. The difference between the mechanisms involved is that under high triaxiality axisymmetric loading the void volume grows rapidly towards coalescence in the localization band, whereas the void in Figs. 8 and 9 has collapsed to a micro-crack long before the onset of localization and the behavior inside the localization band depends on the interaction of neighbouring micro-cracks.

The deformed unit cells in Fig. 5, for $B_0/A_0 = 1$, show nearly as much waviness of the top and bottom of the cell as that found at the initially vertical sides of the cell. This indicated that there is not only interaction between neighboring voids in the transverse direction but also between neighboring voids in the vertical direction. In Fig. 9 this waviness of the top and bottom of the unit cell has nearly disappeared. This is due to the higher stiffness of these parts of the unit cell, which models a larger spacing between the voids in the vertical direction than in the transverse direction.

For $B_0/A_0 = 4$ computations corresponding to different stress states are compared in Fig. 10, with $R_0/A_0 = 0.25$. For $\Sigma_{22} = 0$ two values of the ratio Σ_{11}/Σ_{12} are considered, 0.1 and 0.6. The higher of these values gives a somewhat lower stress maximum, but for both values of the stress ratio Σ_{11}/Σ_{12} final failure is predicted at nearly the same value of the average deformation gradient F_{12}. When there is a tensile stress in the vertical direction, $\Sigma_{22}/\Sigma_{12} = 0.3$, the sensitivity is larger. This stress component reduces the value of F_{12} at final failure, and the reduction is larger for $\Sigma_{11}/\Sigma_{12} = 0.6$ than for $\Sigma_{11}/\Sigma_{12} = 0.1$.

The aspect ratio $B_0/A_0 = 4$ is that considered in the previous articles (Tvergaard, 2008; Tvergaard, 2009), in both cases with zero straining prescribed along the x^1-axis. Therefore, one curve is included in Fig. 10 for which $F_{11} = 0$ is prescribed rather than the value of the transverse stress component Σ_{11}. This curve is computed for $\Sigma_{22} = 0$ and it is seen that the resulting curve differs rather little from the other two curves with $\Sigma_{22} = 0$. In the previous articles the horizontal axis showed the average shear angle ψ, defined by $\tan\psi = (u_D^1 - u_A^1)/2B$, where $2B$ is the current height of the deformed cell. The curve for $F_{11} = 0$ shown in Fig. 10 is in good agreement with the corresponding curve shown in (Tvergaard, 2009), even though the boundary conditions at the top and bottom are not completely identical. The computations in Fig. 10 rely on full periodicity, as described by Eqs. (4) and (5), while simpler boundary conditions at the top and bottom were used in the previous studies.

Fig. 11 again considers the case of $B_0/A_0 = 1$, $R_0/A_0 = 0.25$ and $\rho = 0.15$, including the curve for $\Sigma_{22} = 0$ and $\Sigma_{11}/\Sigma_{12} = 0.1$ also shown in Figs. 4, 6, 7 and 8. While keeping the ratio $\Sigma_{11}/\Sigma_{12} = 0.1$ fixed, the value of Σ_{22}/Σ_{12} is varied. This has rather little effect on the plateau level at the stress maximum, but it is seen that a positive value of Σ_{22} gives earlier final failure, while a negative Σ_{22} delays the occurrence of final failure.

5. Discussion

The unit cell analyzed here, with full periodicity at the sides and at the top and bottom, allows for the study of different initial void spacings in the vertical and horizontal directions and for the effect of different stress states. Most of the computations here are carried out for $B_0/A_0 = 1$, i.e. for equal spacing in the two directions. In these cases all four edges of the unit cell get heavily deformed, as is illustrated by the deformed meshes in Fig. 5. When the macroscopic shear stress Σ_{12} decays rapidly after the maximum, it is clear that shear band localization will develop in the solid, leading to final failure by micro-crack coalescence inside the shear band. However, the assumed periodicity does not allow for representing such a localization mode. In a larger aspect ratio unit cell, as that illustrated in Fig. 9, it is clear that a horizontal shear band develops between adjacent micro-cracks in neighboring unit cells. Due to the assumed periodicity, this prediction actually means a number of parallel shear bands through each layer of adjacent micro-cracks.

Previous studies (Tvergaard, 2008, Tvergaard, 2009) were limited to zero straining in the horizontal direction, $F_{11} = 0$, while here the value of the stress component Σ_{11} can be specified instead. Several analyses here have been carried out for $\Sigma_{22} = 0$ and $\Sigma_{11}/\Sigma_{12} = 0.1$, i.e. for a stress state close to simple shear ($\Sigma_{11} = 0,\ \Sigma_{22} = 0,\ \Sigma_{12} \neq 0$), but also larger tensile or compressive values of Σ_{11} or Σ_{22} have been considered. Generally, an increased stress triaxiality promotes earlier failure, while a negative stress triaxiality tends to delay failure. But the effect of these stress variations is found to be smaller for the low aspect ratio unit cell ($B_0/A_0 = 1$) than for higher aspect ratios, which represent a higher initial void spacing in the vertical direction than in the horizontal direction.

An approximate procedure is applied here to account for crack surface contact after that the void has collapsed to a crack. This

means that the crack is not allowed to close up completely before loads are applied to the crack surfaces to simulate contact forces. Rather little sensitivity has been found to variations of the parameter ρ controlling this artificial amount of opening, which supports the usefulness of the model. However, it is noted that no friction type contact forces are modeled, so the procedure can only represent frictionless sliding of the crack surfaces against each others. The normal contact pressures found in the analyses are sometimes well above the initial yield stress of the material, so friction could play an important role, in particular for cases where a rather large negative stress component Σ_{22} is prescribed. Friction would impede the amount of shear deformations in the cell around the micro crack and thus delay the onset of failure.

In practice voids often nucleate from inclusions or second-phase particles, so that the particles are still present inside the voids. Some of the early analyses of Fleck et al. (1989) accounted for sliding contact between the surfaces of a collapsing void and the contained particle. In analyses carried as far as those in the present study the micro-cracks grow much longer than the particle size, so parts of the micro-crack surface would be in contact with the void, while other parts would be pressed against the opposite crack surface.

The voids considered here are cylindrical and the analyses assume plane strain conditions, while in a real material voids are three dimensional, e.g. close to spherical shapes initially. If full 3D numerical analyses were carried out for unit cells containing such voids subject to shearing, it is expected that also these voids would collapse to micro cracks, and that they would subsequently rotate and elongate until they interact with neighboring micro cracks. In a full 3D specimen the interacting micro cracks would not cover the whole width of the specimen, as in the present plane strain studies, and it is expected that this would much increase the critical value of the shear deformation gradient F_{12}, at which final failure is predicted.

In earlier works for ductile failure under high stress triaxiality there has been some effort on proposing a criterion for the onset of coalescence. Many studies have used a critical value of the void volume fraction (e.g. Koplik and Needleman, 1988; Tvergaard, 1990). There has also been interest in coalescence criteria developed by Thomason (1990), based on limit load analysis in perfect plasticity, which relate to effect of void spacing and void aspect ratio, and to modifications for strain hardening materials (Pardoen and Hutchinson, 2000). In the present studies a critical void volume fraction is not relevant, since the voids have collapsed to micro-cracks long before the load maximum is reached, where plastic flow localization leads to final failure. There is currently no simple model for the onset of failure by the coalescence of the micro-cracks. Some insight could be obtained by limit load analyses for micro-cracks in a perfectly plastic solid, as those of Anderson et al. (1990). However, some further understanding of the micro-crack based failure has been obtained (Tvergaard and Nielsen, 2010) by comparison with predictions of the shear-extended Gurson model of Nahshon and Hutchinson (2008).

References

Anderson, P.M., Fleck, N.A., Johnson, K.L., 1990. Localization of plastic deformation in shear due to microcracks. J. Mech. Phys. Solids 38 (5), 681–699.

Barsoum, I., Faleskog, J., 2007a. Rupture mechanisms in combined tension and shear – Micromechanics. Int. J. Solids Struct. 44, 5481–5498.

Barsoum, I., Faleskog, J., 2007b. Rupture mechanisms in combined tension and shear – Experiments. Int. J. Solids Struct. 44, 1768–1786.

Benzerga, A.A., Leblond, J.-B., 2010. Ductile fracture by void growth to coalescence. Adv. Appl. Mech. 44, 169–305.

Cowie, J.G., Azrib, M.A., Olson, G.B. 1987. Micro-void formation during shear deformation of ultrahigh strength steels. In: Proc. of 34th Sagamore Army Research Conference.

Dahl, J., Nielsen, K.L., Tvergaard, V., 2012. Effect of contact conditions on void coalescence at low stress triaxiality shearing. J. Appl. Mech. ASME 79 (2), 021003.

Danas, K., Castaneda, P. Ponte., 2009a. A finite-strain model for anisotropic viscoplastic media: I – Theory. Eur. J. Mech. A/Solids 28, 387–401.

Danas, K., Castaneda, P. Ponte, 2009b. A finite-strain model for anisotropic viscoplastic media: II – Applications. Eur. J. Mech. A/Solids 28, 402–416.

Fleck, N.A., Hutchinson, J.W., 1986. Void growth in shear. Proc. R. Soc. (Lond.) A407, 435–458.

Fleck, N.A., Hutchinson, J.W., Tvergaard, V., 1989. Softening by void nucleation and growth in tension and shear. J. Mech. Phys. Solids 37 (4), 515–540.

Garrison Jr, W.M., Moody, N.R., 1987. Ductile fracture. J. Phys. Chem. Solids 48 (11), 1035–1074.

Gologanu, M., Leblond, J., Perrin, G., Devaux, J., 1997. Recent extensions of Gurson's model for porous ductile metals. In: Continuum Micromechanics. Springer-Verlag, Berlin, pp. 61–106.

Gurson, A.L., 1977. Continuum theory of ductile rupture by void nucleation and growth – I. Yield criteria and flow rules for porous ductile media. J. Eng. Mater. Technol. 99, 2–15.

Hutchinson, J.W., 1973. Finite strain analysis of elastic-plastic solids and structures. In: Hartung, R.F. (Ed.), Numerical Solution of Nonlinear Structural Problems. ASME, p. 17.

Koplik, J., Needleman, A., 1988. Void growth and coalescence in porous plastic solids. Int. J. Solids Struct. 24, 835–853.

Keralavarma, S.M., Benzerga, A.A., 2010. A constitutive model for plastically anisotropic solids with non-spherical voids. J. Mech. Phys. Solids 58, 874–901.

Leblond, J.-B., Mottet, G., 2008. A theoretical approach of strain localization within thin planar bands in porous ductile materials. C. R. Mecanique 336, 176–189.

Nahshon, K., Hutchinson, J., 2008. Modification of the Gurson model for shear failure. Eur. J. Mech./A Solids 27, 1–17.

Pardoen, T., Hutchinson, J.W., 2000. An extended model for void growth and coalescence. J. Mech. Phys. Solids 48, 2467–2512.

Pedersen, T.Ø., 1998. Remeshing in analysis of large plastic deformations. Comput. Struct. 67, 279–288.

Scheyvaerts, F., Onck, P.R., Bréchet, Y., Pardoen, T. 2006. Void growth and coalescence under general loading conditions. Report, Université catholique de Louvain.

Thomason, P.F., 1990. Ductile Fracture of Metals. Pergamon Press.

Tvergaard, V., 1976. Effect of thickness inhomogeneities in internally pressurized elastic–plastic spherical shells. J. Mech. Phys. Solids 24, 291.

Tvergaard, V., 1981. Influence of voids on shear band instabilities under plane strain conditions. Int. J. Fracture 17, 389–407.

Tvergaard, V., 1990. Material failure by void growth to coalescence. Adv. Appl. Mech. 27, 83–151.

Tvergaard, V., 1997. Studies of void growth in a thin ductile layer between ceramics. Comput. Mech. 20, 186–191.

Tvergaard, V., 2004. On fatigue crack growth in ductile materials by cracktip blunting. J. Mech. Phys. Solids 52, 2149–2166.

Tvergaard, V., 2008. Shear deformation of voids with contact modeled by internal pressure. Int. J. Mech. Sci. 50, 1459–1465.

Tvergaard, V., 2009. Behaviour of voids in a shear field. Int. J. Fracture 158, 41–49.

Tvergaard, V., Nielsen, K.L., 2010. Relations between a micro-mechanical model and a damage model for ductile failure in shear. J. Mech. Phys. Solids 58, 1243–1252.